

1 Physical properties and gas hydrate at a near-seafloor thrust fault, Hikurangi Margin, New

2 Zealand

3 Ann E. Cook<sup>1</sup>, Matteo Paganoni<sup>2</sup>, M. Ben Clennell<sup>3</sup>, David D. McNamara<sup>4</sup>, Michael Nole<sup>5</sup>,

4 Xiujuan Wang<sup>6</sup>, Shuoshuo Han<sup>7</sup>, Rebecca E. Bell<sup>8</sup>, Evan A. Solomon<sup>9</sup>, Demian M. Saffer<sup>7</sup>,

5 Philip M. Barnes<sup>10</sup>, Ingo A. Pecher<sup>11</sup>, Laura M. Wallace<sup>12</sup>, Leah J. LeVay<sup>13</sup> & Katerina E.

6 Petronotis<sup>13</sup>

7 <sup>1</sup>School of Earth Sciences, The Ohio State University, Columbus, Ohio, USA; Corresponding

8 author: [cook.1129@osu.edu](mailto:cook.1129@osu.edu)

9 <sup>2</sup>Department of Earth Sciences, University of Oxford, Oxford, UK & Shell International Global

10 Solutions, Rijswijk, The Netherlands

11 <sup>3</sup>CSIRO, Kensington, Western Australia, Australia

12 <sup>4</sup>Earth, Ocean and Ecological Sciences, University of Liverpool, Liverpool, UK

13 <sup>5</sup>Center for Energy and Earth Systems, Sandia National Laboratories, Albuquerque, New

14 Mexico, USA

15 <sup>6</sup>Institute of Oceanography, Chinese Academy of Sciences, Quidao, China

16 <sup>7</sup>Institute for Geophysics, University of Texas-Austin, Austin, Texas, USA

17 <sup>8</sup>Basins Research Group, Imperial College London, Kensington, UK.

18 <sup>9</sup>School of Oceanography, University of Washington, Seattle, Washington, USA

19 <sup>10</sup>National Institute of Water and Atmospheric Research (NIWA), Wellington, New Zealand

20 <sup>11</sup>School of Environmental and Marine Sciences, University of Auckland, Auckland, New

21 Zealand

22 <sup>12</sup>GNS Science, Lower Hutt, New Zealand

23 <sup>13</sup>International Ocean Discovery Program, Texas A&M University, College Station, Texas, USA

24

25

26 **Key Points**

27 The Pāpaku fault zone is a 33-m thick near-seafloor splay fault drilled at Site U1518 on the

28 Hikurangi Margin

29 Multiple lines of observational, geophysical and geochemical evidence suggest that there is little

30 to no fluid flow along the Pāpaku fault

31

32 **Abstract**

33 The Pāpaku fault zone, drilled at IODP Site U1518, is an active splay fault in the frontal

34 accretionary wedge of the Hikurangi Margin. In logging-while-drilling data, the 33 m-thick fault

35 zone exhibits mixed modes of deformation associated with a trend of downward decreasing

36 density, P-wave velocity and resistivity. Methane hydrate are observed from ~30-585 mbsf,

37 including within and surrounding the fault zone. Hydrate accumulations are vertically

38 discontinuous and occur throughout the entire logged section at low to moderate saturation in

39 silty and sandy cm-thick layers. We argue that the hydrate distribution implies that the methane

40 is not sourced from fluid flow along the fault but instead by local diffusion. This, combined with

41 geophysical observations and geochemical measurements from Site U1518, suggests that the

42 fault is not a focused migration pathway for deeply-sourced fluids and that the near-seafloor

43 Pāpaku fault zone has little to no active fluid flow.

44

45

46

47

## 48 **Plain Language Summary**

49 Faults are boundaries in the Earth where two different blocks of sediment or rock slide past each  
50 other. Offshore New Zealand, the Pāpaku Fault is very shallow and intersects the seafloor but  
51 connects to deeper faults kilometers below the seafloor where large earthquakes can occur. An  
52 ice-like form of methane called hydrate also occurs within and surrounding the fault. We use  
53 scientific drilling data to understand the physical properties of the fault. Hydrate can affect fault  
54 properties and how fluid flows; however, based on the pattern of hydrate distribution and other  
55 geochemical and geophysical measurements we suggest that the Pāpaku fault does not have  
56 active fluid flow.

57

58 **Keywords:** Hikurangi Margin, fault, gas hydrate, accretionary wedge

59

## 60 **1. Introduction**

61 The physical and hydrological properties of subduction zone thrust faults are of great  
62 interest because of their relationship with large earthquakes. Movement along these faults span a  
63 range of behaviors from large earthquakes, to slow and low frequency earthquakes, to aseismic  
64 creep behavior [*Hyndman et al., 1997; Rogers and Dragert, 2003*]. A number of variables  
65 influence this spectrum of slip behavior, such as temperature, frictional properties, effective  
66 stress and pore pressure [*Beroza and Ide, 2011; Saffer and Wallace, 2015; Bürgmann, 2018*]. In  
67 addition, fault slip behavior near the trench of subduction zones is critical to understand as these  
68 areas can generate large tsunamis [*Ide et al., 2011*]. The fluid flow and drainage patterns of  
69 active faults play an important role in mediating the distribution of fluid pressure and effective

70 stress. These flow patterns are also a first-order control on seepage, dewatering processes, and  
71 volatile fluxes in subduction forearcs [e.g. *Moore and Vrolijk*, 1992; *Carson and Screaton*, 1998;  
72 *Saffer and Tobin*, 2011].

73 At the Hikurangi Margin along the eastern North Island of New Zealand, the Pacific plate  
74 subducts westward beneath the Australian plate at a rate of ~35-55 mm/year. A range of fault  
75 slip styles have been observed or inferred along the Hikurangi Margin including short-term and  
76 long-term slow-slip events (SSE), earthquakes, and tsunami earthquakes [*Doser and Webb*,  
77 2003; *Wallace et al.*, 2009, 2012]. Moreover, SSEs at the northern Hikurangi Margin have been  
78 observed within 2 km of the seafloor, and these are among the shallowest SSE observations on  
79 Earth [*Wallace et al.*, 2016]. The variety of slip styles on the Hikurangi Margin, opportunities  
80 for near-field monitoring of SSEs near the trench, and the accessibility of the SSE source to  
81 scientific ocean drilling and seismic imaging, makes the area an excellent location to study fault  
82 structure, fault properties and fluid flow.

83 The Pāpaku fault (Figure 1), drilled at International Ocean Discovery Program (IODP)  
84 Site U1518, intersects the seafloor in a highly active part of the outer margin. The fault is part of  
85 a splay system in the accretionary wedge that connects to the deep décollement 10-25 km  
86 landward of the drill site, and 2-3 km deeper [*Barker et al.*, 2018]. While the Pāpaku fault zone  
87 has been penetrated at very shallow depths at the drilling location (~315 meters below seafloor,  
88 mbsf) it may slip and may exhibit pore pressure and fluid flow changes as a result of SSEs.

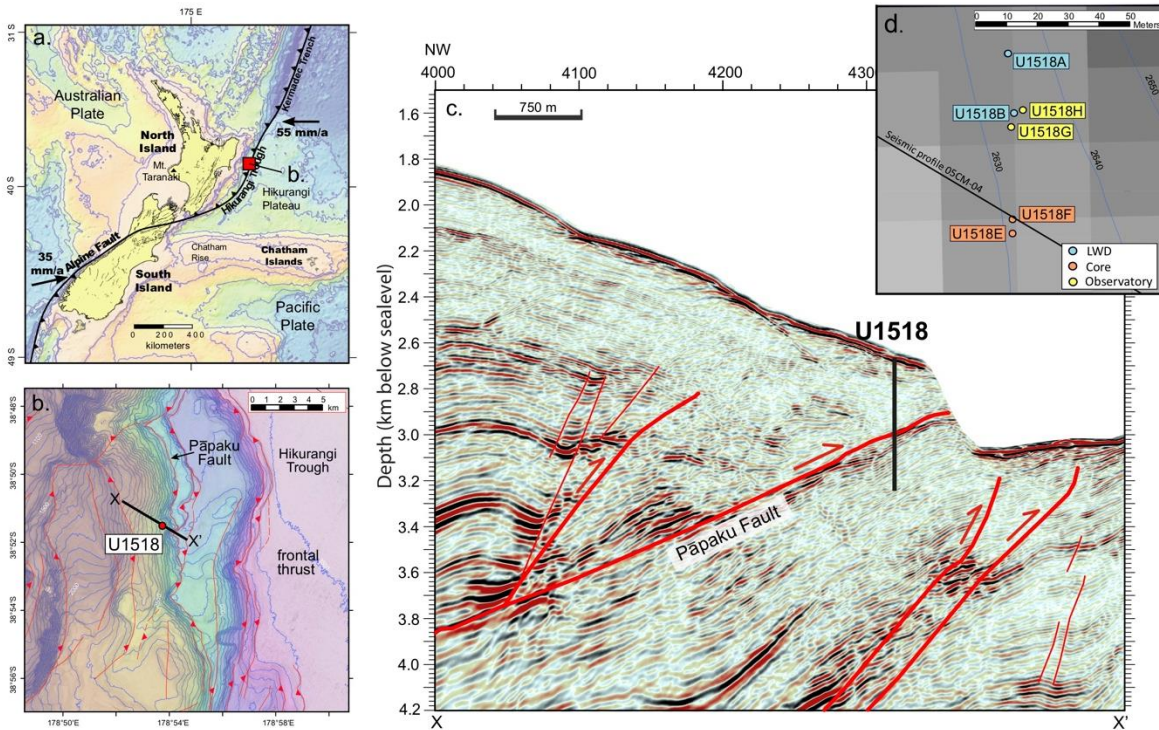
89 An extensive suite of *in situ* measurements were collected across the Pāpaku fault in Hole  
90 U1518B using logging-while-drilling (LWD) tools during IODP Expedition 372 (Figure 1)  
91 [*Saffer et al.*, 2019b]. About 50 m to the south, the Pāpaku fault was cored at Hole U1518F  
92 during Expedition 375 (Figure 1). There was 43% core recovery over a ~300 m interval

93 surrounding the fault [*Saffer et al.*, 2019b] and 33% recovery in the fault zone [*Fagereng et al.*,  
94 2019]. While this core recovery is comparable to other fault zones, coring alone leaves  
95 significant gaps in the characterization of the Pāpaku fault zone and surrounding sedimentary  
96 system that can be resolved with continuous LWD measurements.

97 Methane hydrate, a solid clathrate of methane and H<sub>2</sub>O [*Sloan and Koh*, 2007] was  
98 observed in core at Site U1518 at several different intervals from 33-391 mbsf using infrared  
99 scanning and pore water chlorinity measurements [*Saffer et al.*, 2019b]. Methane hydrate is stable  
100 throughout Site U1518; the top of methane hydrate stability occurs at ~600 m below sea level in  
101 the water column (water depth is ~2630 m) and the base of the methane hydrate stability occurs at  
102 ~585 mbsf, using the CSMHyd software [*Sloan and Koh*, 2007] which incorporates measured  
103 temperature, background pore water salinity, and estimated pressure [*Saffer et al.*, 2019b].  
104 Hydrate can affect fluid flow patterns by influencing sediment permeability and pore pressure  
105 [*Nimblett and Ruppel*, 2003; *Xu and Germanovich*, 2006; *Sultan*, 2007; *Daigle et al.*, 2015] as well  
106 as alter the sediment physical properties such as increasing stiffness, cohesion and shear strength  
107 [*Pearson et al.*, 1983; *Yun et al.*, 2005; *Waite et al.*, 2009; *Yoneda et al.*, 2017].

108 The Pāpaku fault now hosts a borehole observatory installed in Hole U1518H (only a few  
109 meters from Hole U1518B) that is monitoring pore fluid pressure, fluid flow rates and  
110 temperature, as well as sampling fluids for geochemical analyses [*Saffer et al.*, 2019b].  
111 Therefore, the logging and coring datasets collected at Site U1518 yield insight into the  
112 properties of the Pāpaku fault, surrounding sediment, hydrate distribution, and the fluid flow  
113 system that provides valuable context for the interpretation of fault slip processes and the  
114 observatory data [e.g. *Sawyer et al.*, 2008; *Kinoshita et al.*, 2018]. Herein, we interpret LWD

115 measurements from Hole U1518B and use the distribution of hydrate to infer fluid flow within  
116 and around the Pāpaku fault zone.



117  
118 Figure 1. a) Location of Site U1518 offshore the North Island of New Zealand in the  
119 Hikurangi Margin. b) Zoomed in bathymetry near the Pāpaku Fault. c) Seismic cross section over the area,  
120 with ancillary faults and the Pāpaku Fault identified with red lines. Seismic line location shown  
121 in b (black line). d) The placement of six holes at Site U1518. All images are modified from  
122 *Saffer et al.*, [2019a; 2019b]. LWD = logging while drilling.

123

## 124 2. Methods

125 A comprehensive set of *in situ* LWD measurements were collected across the Pāpaku  
126 fault in Hole U1518B, which included natural gamma ray, ultrasonic caliper, neutron porosity,  
127 source-less neutron density, button, ring and propagation resistivity measurements, resistivity

128 imaging, P-wave and S-wave velocity, nuclear magnetic resonance (NMR) porosity and NMR T<sub>2</sub>  
129 relaxation time distribution [Wallace *et al.*, 2019]. Figure 2 depicts selected measurements  
130 across the fault zone from Hole 1518B.

131 We used Schlumberger’s petrophysical analysis software, Techlog, to orient and interpret  
132 statically and dynamically normalized resistivity images to identify bedding, fault and fractures  
133 orientations [e.g. Wallace *et al.*, 2019]. We also interpreted deformation features in the image,  
134 which we define as either non-throughgoing sinusoids fragmented due to deformation, or  
135 throughgoing features that change orientation on the image (for example, features appear  
136 squeezed and a symmetric sinusoid cannot be fit to the feature), which indicate possible soft-  
137 sediment deformation.

138 We adapt Archie’s equation [Archie, 1942] to calculate hydrate saturation,  $S_h$ , which is  
139 applicable when hydrate is in the primary pore space of water wet sands and silts [Spangenberg,  
140 2001; Goldberg *et al.*, 2010; Priegnitz *et al.*, 2015; Cook and Waite, 2018]. We use RING  
141 resistivity,  $R_{RING}$ , and an estimated background resistivity,  $R_o$ , to calculate  $S_h$ :

$$142 \quad S_h = 1 - \left( \frac{R_o}{R_{RING}} \right)^{1/n} \quad \text{Equation 1}$$

143 We estimate  $R_o$  by carefully considering the background trends in resistivity, P-wave velocity,  
144 neutron porosity and NMR porosity; we also conservatively overestimated  $R_o$  in intervals with  
145 borehole washout.  $R_{RING}$  is used in saturation calculations because it is the most sensitive  
146 resistivity measurement for hydrate in cm-thick layers due to the high vertical resolution (5-8  
147 cm) for depth of penetration [Cook *et al.*, 2012]. For the saturation exponent,  $n$ , we apply  $n = 2$  &  
148  $n = 3$  to show the probable range of hydrate saturations [Cook and Waite, 2018]. We also

149 calculated  $R_o$  from neutron porosity for comparison, but we did not use it for saturation  
150 calculations (see Supporting Information).

151 Other than hydrate, sediment overcompaction or cementation could cause spikes in  
152 resistivity, but 1) cements are not observed in the core at Site U1518 [Saffer *et al.*, 2019b] and 2)  
153 there is no decrease in neutron porosity or NMR porosity indicating cementation or  
154 overcompaction at the locations of any of the thicker resistivity spikes; thus hydrate the most  
155 likely cause of resistivity exceeding  $R_o$  throughout Site U1518.

156

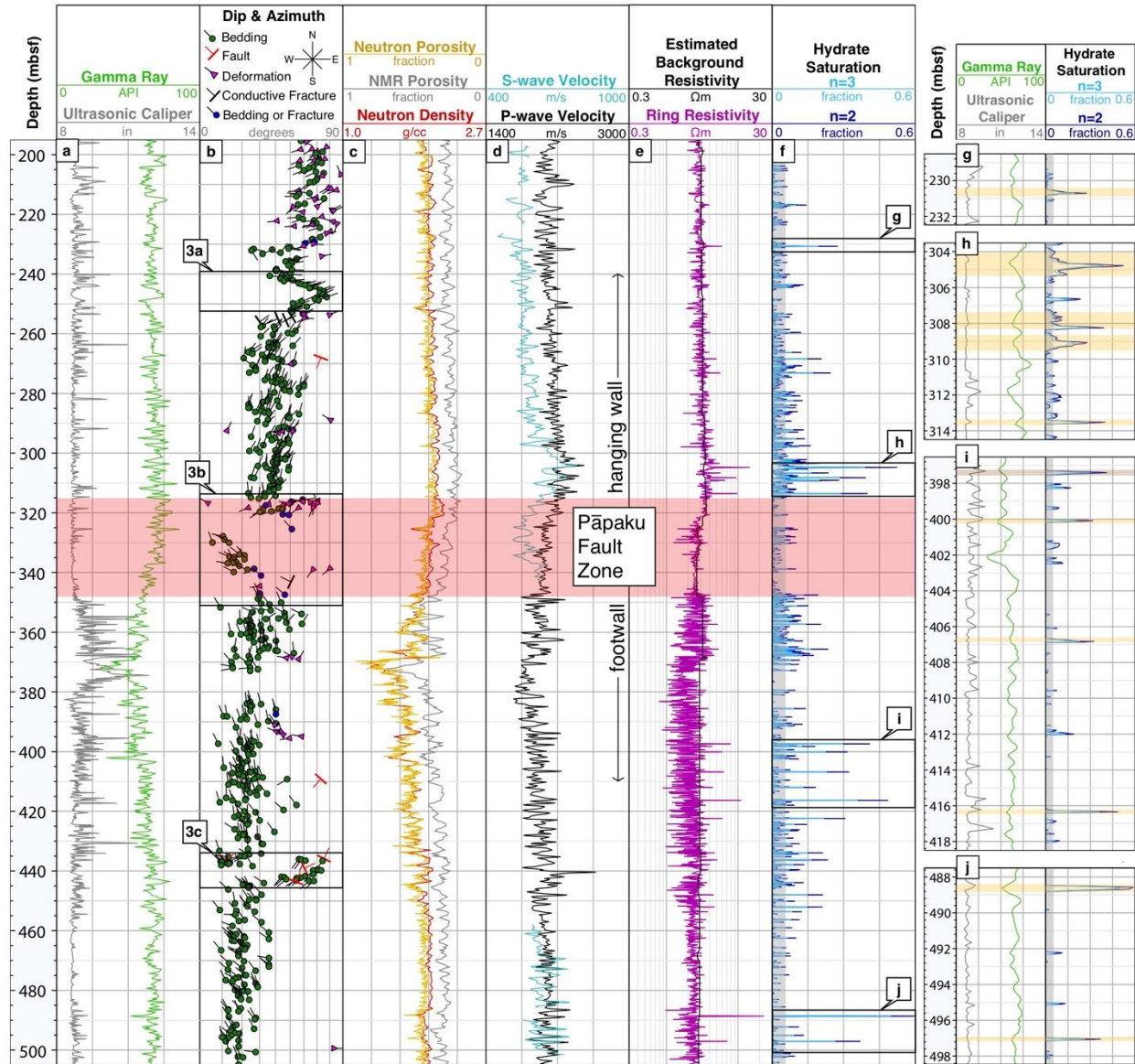
### 157 **3. The Pāpaku fault zone & surrounding system**

158 In the LWD data, we observe significant changes in the physical properties and bedding  
159 orientation above, below and within the Pāpaku fault zone (Figure 2), which are described in the  
160 following section. Overall, more deformation features are identified in the hanging wall (Figure  
161 2), which may explain the acoustic transparency in the hanging wall relative to the footwall on  
162 seismic data (Figure 1c).

163 On the LWD data, we observe hydrate concentrated in thin layers (on the order of cm to  
164 10's of cm) above, below and within the Pāpaku fault zone (Figure 2). Centimeter to tens of cm-  
165 thick coarse-grained (sand and silt) layers were observed throughout Site U1518 in cores [Saffer  
166 *et al.*, 2019b]. We identify these coarse-grained layers on LWD data by local gamma ray lows,  
167 and note that almost all layers with  $S_h > 0.2$  is associated with a local gamma ray low (Figure 2).  
168 While there is variation in hydrate concentrations with depth, there is not a large difference in the  
169 concentration of hydrate filled layers in the hangingwall, fault zone and footwall (Figure 2). Some  
170 of the variation may be due to the occurrence of coarse-grained layers. The fault zone itself does



171 have lower hydrate saturations ( $<0.1$ ) than the immediate surrounding hanging wall and footwall,  
 172 however, other sections such as 235-263 mbsf in the hanging wall and 455-485 mbsf in the  
 173 footwall also have similar low hydrate saturations ( $<0.1$ ).



174  
 175 Figure 2. a. Logging-while-drilling (LWD) well log measurements (Tracks a, c, d & e), image  
 176 interpretation (Track b), estimated background resistivity (Track e) and calculated hydrate  
 177 saturation (Track f) at Hole U1518B. Note that the neutron porosity and neutron density may not  
 178 provide accurate measurements in this high porosity, clay rich environment, and NMR porosity  
 179 measurements are affected by the presence of gas hydrate. When resistivity is low and close to  
 180 the background, calculated hydrate saturations (Track f) have lower confidence; we grayed these  
 181 lower confidence saturations. At low resistivity, intervals without hydrate could be identified  
 182 with low saturation and intervals could be incorrectly identified as water-saturated. Insets g, h, i

183 and j show enlarged intervals in U1518B in thin layers. All layers greater than ~20% that are  
184 associated with gamma ray lows are highlighted in yellow on the insets (10 layers); one layer  
185 that was not associated with a gamma ray low was highlighted in brown on Inset i.

186  
187

### 3.1 Hanging wall and fault zone

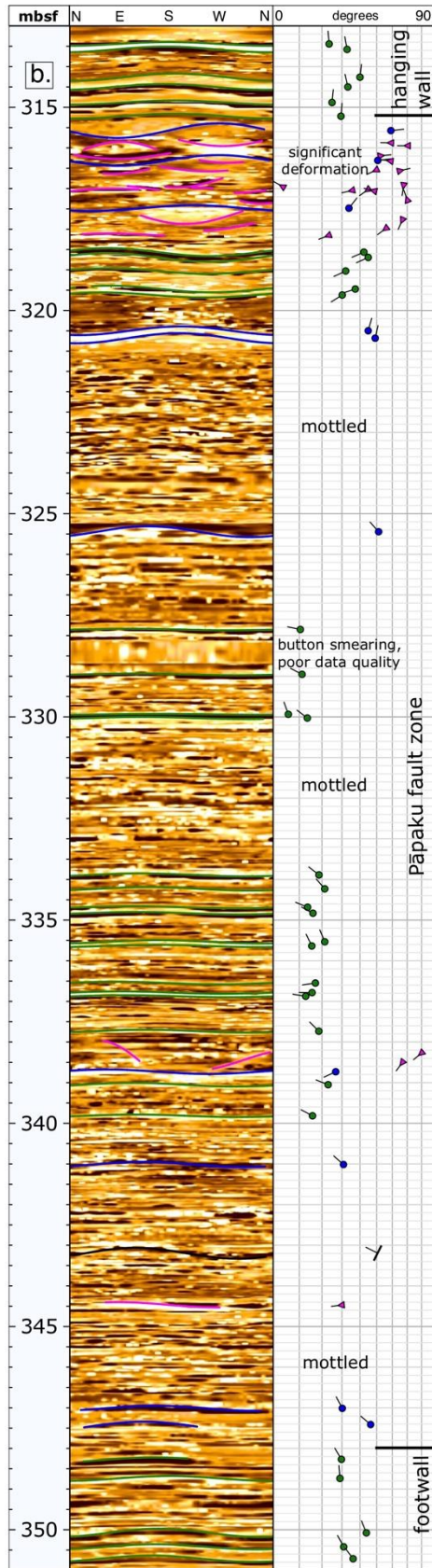
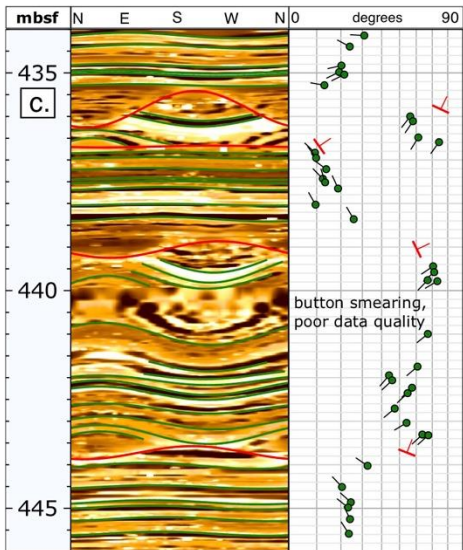
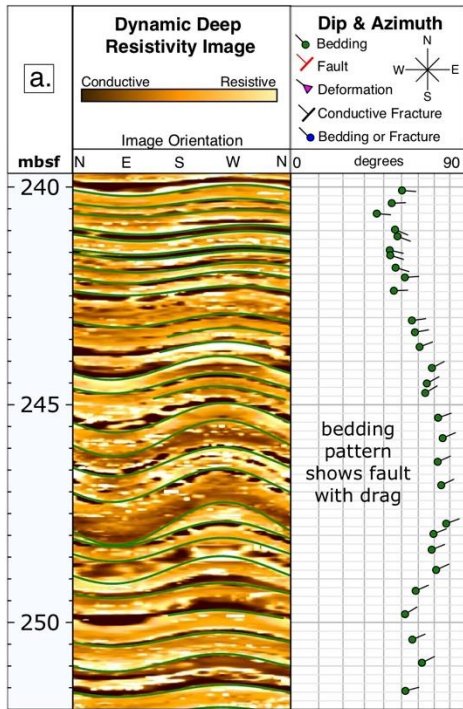
188 In core from Hole U1518F, the Pāpaku fault zone was identified from 304-361 mbsf,  
189 which includes an ~18 m-thick fault zone underlain by ~30 m of less deformed material,  
190 followed by a ~10 m-thick subsidiary fault zone [Fagereng *et al.*, 2019]. The Pāpaku fault zone  
191 depths are different in LWD Hole U1518B ~50 m to the north, where we interpret the base of the  
192 hanging wall and the top of the Pāpaku fault zone to begin 11 meters deeper, at 315 mbsf, where  
193 there is an abrupt change from 25-45° north-dipping beds to a chaotically oriented and deformed  
194 interval (Figure 3b) [Fagereng *et al.*, 2019; Saffer *et al.*, 2019].

195 The base of the hanging wall (300-315 mbsf) is marked by elevated P-wave and S-wave  
196 velocity and low neutron porosity. Increased compaction and shear strengthening from fault  
197 movement compared to the adjacent intervals may explain such trends. However, this interval  
198 also hosts hydrate (Figure 2b), which contributes to the increase in P-wave and S-wave velocity  
199 by increasing the cohesive and mechanical strength. The hydrate is occurring at saturations up to  
200 0.5 in 10's of cm-thick layers that are generally coarser-grained (Figure 2h).

201 The bedding orientation from the hanging wall (dipping 25-45° north) is truncated  
202 against chaotically dipping features which are a combination of deformation, fractures and  
203 bedding (Figure 3b). The interval between 315-321 mbsf has the highest density values in the  
204 hole, likely related to increased compaction caused by fault movement, though the P-wave and  
205 S-wave velocity are lower than the interval just above that contains hydrate (Figure 2).

206 Most of the fault zone in Hole U1518B is marked by a gradual decrease in P-wave  
207 velocity, resistivity and neutron density with depth. These LWD measurements are of high  
208 quality in the fault zone as the borehole diameter is close to the bit size, however, bedding and  
209 fracture orientation is often difficult to distinguish within the fault zone as the image appears  
210 mottled (Figures 2 & 3). A variety of deformation features were observed in the core, including  
211 breccia, flow banding, breccia clasts, dismembered beds, small faults and fractures [*Fagereng et*  
212 *al.*, 2019]. The mottled appearance observed on the image logs over several large sections in the  
213 fault zone (Figure 3b) are likely caused by discontinuous deformation features smaller than  
214 several horizontal image bins (~3-5 cm) and the vertical resolution (~5-8 cm) of the resistivity  
215 images [*Luthi*, 2001; *Schlumberger*, 2007]. Bright white mottled features on the image log  
216 (Figure 3b) may also be hydrate forming in nodules or in deformed coarser-grained layers within  
217 the fault zone. Intervals in the fault zone with identified bedding may be a relatively intact  
218 section within the fault zone or could be deformed beds or flow banding.

219 Below ~335 mbsf, the gamma ray (Figure 2) and NMR T2 distribution (shown in [*Saffer*  
220 *et al.*, 2019b]) indicate sediment gradually grades into a nearly 100 m-thick, coarse-grained unit  
221 of silts and sands with thin mud interbeds; the bottom of the fault zone is near the top of this  
222 coarse-grained unit at 340-348 mbsf.



224 Figure 3. Selected resistivity image log intervals and interpretation from Hole U1518B. a)  
225 Bedding patterns indicating a thrust fault propagation fold, b) the Pāpaku fault zone and c) a  
226 section of faults and offset beds in the footwall. Higher resolution image logs and interpretation  
227 are available in Supporting Information (Figure S1).

228  
229

### 3.2 Footwall

230 The base of the Pāpaku fault zone and the transition to the footwall is not as clear as the  
231 hanging wall transition on LWD data. Part of this ambiguity is due to the lithology, as grading  
232 into coarser sediments is indicated by the gamma ray beginning at ~335 mbsf, making it difficult  
233 to distinguish between physical property changes from coarsening sediment versus changes  
234 produced by deformation processes within the fault zone. Core observations note silts and  
235 hemipelagic mud at the bottom the fault zone and the top of the footwall, however, core recovery  
236 was low in the footwall (<36%) which may be due to coarser-grained sands and silts being  
237 washed out during drilling [Saffer *et al.*, 2019b].

238 We argue the most likely depth for the base of the Pāpaku fault zone on LWD data is  
239 340-348 mbsf. At this depth, there are only a few features identified on the image logs (Figure  
240 3), suggesting the interval may still be affected by fault-related deformation. The contrasting  
241 bedding orientations above 340 and below 348 mbsf further suggests there is deformation  
242 occurring in this interval. Below 348 mbsf, most identified beds have a similar orientation to  
243 beds significantly below the fault zone (i.e. from ~450-500 mbsf) indicating that this is the  
244 footwall.

245

246 3.3 Subsidiary faults

247           There are several subsidiary faults and fault-related features visible on the LWD  
248 resistivity images. Six faults identified at 272, 409, 436, 437, 439, and 444 mbsf are dipping  
249 between 12-75° (Figure 2). Figure 3c shows four of these faults, which occur between 435-445  
250 mbsf and are associated with sharp changes in bedding orientation above and below the fault  
251 sinusoid. We cannot identify the relative movement of these faults because beds cannot be  
252 correlated above and below the fault plane sinusoid. This also means that the throw is more than  
253 the amplitude of the sinusoid in the borehole (between 10-100 cm).

254           A major fault zone was interpreted at 351-361 mbsf in coring Hole U1518F [*Fagereng et*  
255 *al.*, 2019] and at 369 mbsf in LWD Hole U1518B [*Saffer et al.*, 2019b]. LWD evidence for a  
256 fault near 369 mbsf includes changing bedding orientations from 368-370 mbsf with some  
257 deformation features; however, there is no clear fault plane like other subsidiary faults observed  
258 in the resistivity images (Figure 3c). In addition, there are several depths (e.g. 226, 234, and 355  
259 mbsf) where bedding orientation changes suddenly which could also be evidence for additional  
260 faults.

261           Another fault-related feature is the orientation of beds from 242-250 mbsf (Figure 3a),  
262 which increase in dip from 242 mbsf and reach the highest angle dip of almost 80° at ~247 mbsf  
263 and then decreases. This pattern of increasing and decreasing dip is consistent with a thrust  
264 fault-propagation fold as well as the stress regime in the hanging wall.

265

#### 266 **4 Discussion**

267           On LWD data from Hole U1518B, we interpret an apparent 33 m-thick Pāpaku fault zone  
268 from 315-348 mbsf. From core in Hole U1518F, *Fagereng et al.* [2019] interpreted the fault



269 zone over an apparent 58 m-thick interval from 304-361 mbsf. The top of the fault zone is  
270 identified in both LWD and core datasets by a low porosity interval at the base of the hanging  
271 wall and at the top of the fault zone [Saffer *et al.*, 2019a]. The difference in the Pāpaku fault zone  
272 thickness and the top of the fault zone may be the result of a variety of different factors [Saffer *et*  
273 *al.*, 2019b]. There may be a change in fault geometry and thickness over the 50 m distance  
274 between holes due to splays or imbricate structure, or poor core recovery may cause an  
275 overestimate of fault thickness in the coring hole. Small differences in fault thickness may also  
276 be related to borehole deviation.

#### 277 4.1 Fluid flow and gas hydrate

278 Hydrate is inferred in many thin, cm- to 10's of cm-thick coarse-grained sediments  
279 throughout Site U1518, from as shallow as ~33 mbsf in core samples [Saffer *et al.*, 2019a] to nearly  
280 total depth (590 mbsf) on LWD data (Figure 2 & S2). Such a frequent occurrence of hydrate  
281 implies that the dissolved pore water methane concentration is very close to solubility throughout  
282 the site, yet hydrate appears to preferentially form in higher concentrations in coarse-grained  
283 sediments with less hydrate in marine muds.

284 This pattern of hydrate-bearing coarse-grained layers interbedded within water-saturated  
285 or low-hydrate saturation marine muds has been observed in several locations, such as accretionary  
286 prisms in the northern Cascadia Margin, the Andaman Sea, and the Nankai Trough as well as in  
287 the Gulf of Mexico [Malinverno, 2010; Cook and Malinverno, 2013; Malinverno and Goldberg,  
288 2015]. The pattern can be explained by a diffusion-dominated methane migration, which is driven  
289 by the difference in methane solubility between coarse-grained sands (or silts) and marine muds  
290 [Malinverno, 2010; Nole *et al.*, 2017; Vanderbeek and Rempel, 2018]. The solubility threshold is

291 higher in muds due the high curvature of the pore surface in small pores [*Clennell et al.*, 1999;  
292 *Rempel*, 2011]. In marine muds near the seafloor, methane can be generated through a series of  
293 microbial reactions, and it is dissolved in the pore water. This methane diffuses into adjacent sand  
294 layers over time, and when the solubility threshold is reached, hydrate forms in the sands first.  
295 Because methane solubility is lower in the sands, this allows for a diffusive flux of methane  
296 dissolved in pore water from marine muds both above and below the sand layers, which can  
297 continue to occur as hydrate forms. Eventually, this leads to significant hydrate saturation in thin  
298 sands surrounded by water-saturated marine muds. Because the methane generated in the muds  
299 only diffuses a few centimeters to meters to fill the thin sands, the mechanism is referred to as  
300 short-migration [*Malinverno*, 2010].

301         Yet, in accretionary wedge environments advective methane fluxes along faults are  
302 observed at many locations worldwide [*Moore and Vrolijk*, 1992; *Kastner et al.*, 1998, 2014;  
303 *Geersen et al.*, 2016] as well as observed and inferred along the Hikurangi Margin, often associated  
304 with gas hydrate systems on seismic data [*Pecher et al.*, 2010; *Crutchley et al.*, 2011; *Plaza-*  
305 *Faverola et al.*, 2012; *Kroeger et al.*, 2015; *Watson et al.*, 2019]. In addition, the Pāpaku fault  
306 zone at Site U1518 does have relatively high porosity (>0.4) in deformed and fractured sediment  
307 which could facilitate fluid flow.

308         We argue, however, that there is combined observational, geochemical, geophysical and  
309 petrophysical evidence supporting little to no advection of deeply-sourced, gas-bearing or  
310 geochemically distinct fluids along the Pāpaku fault zone. First, methane to ethane ratios in  
311 headspace gas samples are greater than 20,000, suggesting that a microbial origin for the methane  
312 is more likely than a deeply-sourced thermogenic origin [*Saffer et al.*, 2019b]. We recognize that



313 thermogenic methane can be microbially altered and microbial methane can be generated rather  
314 deep in some systems and advected upward (for example, modeling suggests microbial generation  
315 peaks at 1600 mbsf in the Pegasus Basin in the southern Hikurangi Margin [*Kroeger et al.*, 2015]).  
316 Even so, an in-situ microbial origin for the methane forming hydrate appears more in line with the  
317 observed pattern of hydrate distribution.

318         At Site U1518, if the methane originated from fluid or gas flow along the Pāpaku fault one  
319 would expect hydrate to occur within and around the fault zone, or perhaps in other large  
320 permeable layers like the coarse-grained unit from ~345-440 mbsf. In addition, it is likely that  
321 hydrate would form at high-concentration in fractures or veins, as they commonly do in other  
322 focused flow settings [*Weinberger and Brown*, 2006; *Abegg et al.*, 2007; *Riedel et al.*, 2010; *Kim*  
323 *et al.*, 2013]; however, there is no evidence for hydrate in veins or fractures on resistivity images  
324 or measurements in Hole U1518B. While we observe an increase in hydrate concentration  
325 immediately surrounding the fault zone (Figure 2), the overall saturation is still moderate to low,  
326 and we also observe that hydrate occurs throughout the site (from ~30 to 590 mbsf) in thin, discreet  
327 layers on the order of cm to 10s of cm-thick. This distribution of hydrate implies that either the  
328 fault zone is not the only source of methane or that the fault zone is not related to the methane  
329 hydrate distribution.

330         Other sources of evidence indicate that there is no active fluid flow along the Pāpaku fault.  
331 Pore water solute profiles indicated there is no evidence for fluid flow along the fault and the  
332 absence of diagenetic cements at Site U1518 further support the lack of fluid advection [*Saffer et*  
333 *al.*, 2019b]. In seismic data, high amplitude, reversed seafloor-polarity reflections from the  
334 decollement and other thrust faults on subduction margins have been linked to possible evidence

335 of fluid flow and/or high pore pressure in both observations and in models [*Moore et al.*, 1995;  
336 *Bangs et al.*, 1999, 2015; *Saffer and Tobin*, 2011]. At the Pāpaku fault, the reverse-seafloor  
337 polarity reflection can be produced by the reduction in both P-wave velocity and density from the  
338 hanging wall into the fault zone (Figure 2), as shown by the synthetic seismogram in *Saffer et al.*,  
339 [2019b]. Therefore, fluid flow and high pore pressure are not required at Site U1518 to explain  
340 the negative impedance on seismic data, and the impedance can be explained by changes in  
341 physical properties. In addition, a 2D high-resolution full waveform inversion P-wave velocity  
342 model by *Gray et al.*, [2019] showed that some fault zones in the wedge are associated with  
343 velocity reductions of up to 500 m/s. The smaller velocity reduction of ~100 m/s in the Pāpaku  
344 fault zone in the *Gray et al.* [2019] model indicates that the fault may not be acting as a significant  
345 conduit for fluid flow in the same way as inferred for other faults.

346 Collectively, multiple lines of evidence suggest the shallow part of the Pāpaku fault zone  
347 currently has low or no fluid advection; however, we cannot rule out fluid flow at greater depths  
348 or brief pulses of fluids along the shallow fault zone in the past. If pulsing occurred in the past,  
349 the fluids are likely through-going and not interacting with the surrounding footwall and hanging  
350 wall system.

351 Although evidence for long distance migration of fluids is fairly common from drilling  
352 frontal thrust faults at subduction zones, another example of a location where there is limited  
353 evidence for fluid flow and methane flux is along the Kumano transect on the Nankai Trough  
354 [*Screaton et al.*, 2009]. Together, the Kumano and Hikurangi sites suggest that inactive or lower  
355 advection hydrologic systems along frontal thrusts could be a more common occurrence than  
356 previously thought. How shallow faults without advection may or may not relate to the deeper

357 fault system is unknown. In the future, data and fluid samples recovered from the borehole  
358 observatory installed at Site U1518 will provide direct constraints on in situ near-seafloor fluid  
359 flow rates and fault zone hydrologic properties of the Pāpaku fault zone.

360

361

## 362 **5 Conclusions**

363         Understanding physical properties and fluid flow around subduction fault zones is essential  
364 for illuminating the role of fluids in fault mechanics and slip behavior. Herein, we argue that the  
365 Pāpaku fault zone does not have significant fluid flow in the near-seafloor system. The 33 m-thick  
366 fault zone does have high porosity and a trend of decreasing P-wave velocity from top to bottom  
367 of the fault. Despite high porosity measured within the fault zone and the occurrence of methane  
368 hydrate in thin sands and silts at Site U1518, we argue that advective fluid flow is likely not causing  
369 the unconnected but frequent occurrence of gas hydrate from 30 to 585 mbsf on logging-while-  
370 drilling (LWD) data. Instead we argue that the hydrate distributed in coarse-grained layers less  
371 than 1 m-thick is caused by local diffusion of microbially generated methane. This further supports  
372 evidence from geochemical analysis on pore water samples and modeling work on seismic data  
373 that the Pāpaku fault does not have significant active fluid flow.

374

375

## 376 Acknowledgements

377 This research used data and samples provided by the International Ocean Discovery Program  
378 (IODP) and the data in this paper can be accessed through IODP's database

379 ([http://mlp.ldeo.columbia.edu/logdb/scientific\\_ocean\\_drilling/](http://mlp.ldeo.columbia.edu/logdb/scientific_ocean_drilling/)). We gratefully acknowledge  
380 IODP, Texas A&M university staff, Schlumberger Drilling & Measurements, the crew of the *JR*,  
381 and the Expedition 375 and 372 science parties. We thank Schlumberger for the Techlog software  
382 donation. We thank A. Malinverno and G. Guerin for their comments and suggestions on this  
383 paper.

384 Cook was supported by NSF Award 1752882, Paganoni was funded by NERC Grant  
385 NE/R016615/1 and Bell from NERC Grant NE/S00291X/1, Wang was supported by National  
386 Natural Science Foundation of China (41976077), and McNamara was supported by the  
387 Geological Survey Ireland. Barnes and Wallace acknowledge support from the New Zealand  
388 Endeavour fund, Contract CO5X1605, as well as NIWA and GNS SSIF core funding. LeVay and  
389 Petronotis were supported by IODP-JRSO NSF Award 1326927.

390

391 \_\_\_\_\_

- 392 Abegg, F., G. Bohrmann, J. Freitag, and W. Kuhs (2007), Fabric of gas hydrate in sediments  
393 from Hydrate Ridge - Results from ODP Leg 204 samples, *Geo-Marine Lett.*, 27(2–4), 269–  
394 277, doi:10.1007/s00367-007-0080-4.
- 395 Archie, G. E. (1942), The electrical resistivity log as an aid in determining some reservoir  
396 characteristics, in *Transactions of the American Institute of Mining and Metallurgical*  
397 *Engineers*, Vol. 146, pp. 54–63.
- 398 Bangs, N. L., K. D. McIntosh, E. A. Silver, J. W. Kluesner, and C. R. Ranero (2015), Fluid  
399 accumulation along the Costa Rica subduction thrust and development of the seismogenic  
400 zone, *J. Geophys. Res. Solid Earth*, 120, 67–86, doi:10.1002/2014JB011265.
- 401 Bangs, N. L. B., T. H. Shipley, J. C. Moore, and G. F. Moore (1999), Fluid accumulation and  
402 channeling along the northern Barbados Ridge Decollement thrust, *J. Geophys. Res. Solid*  
403 *Earth*, 104, 20399–20414, doi:10.1029/1999JB900133.
- 404 Barker, D. H. N., S. Henrys, F. Caratori Tontini, P. M. Barnes, D. Bassett, E. Todd, and L.  
405 Wallace (2018), Geophysical Constraints on the Relationship Between Seamount  
406 Subduction, Slow Slip, and Tremor at the North Hikurangi Subduction Zone, New Zealand,  
407 *Geophys. Res. Lett.*, 45(23), 12,804–12,813, doi:10.1029/2018GL080259.
- 408 Beroza, G. C., and S. Ide (2011), Slow Earthquakes and Nonvolcanic Tremor, *Annu. Rev. Earth*  
409 *Planet. Sci.*, 39(1), 271–296, doi:10.1146/annurev-earth-040809-152531.

410 Bürgmann, R. (2018), The geophysics, geology and mechanics of slow fault slip, *Earth Planet.*  
411 *Sci. Lett.*, 495, 112–134, doi:10.1016/j.epsl.2018.04.062.

412 Carson, B., and E. J. Screaton (1998), Fluid flow in accretionary prisms: Evidence for focused,  
413 time-variable discharge, *Rev. Geophys.*, (36), 329–351,  
414 doi:https://doi.org/10.1029/97RG03633.

415 Clennell, M. Ben, M. Hovland, S. Booth, H. Pierre, and J. Winters (1999), Formation of Gas  
416 Hydrate in Marine Sediments: 1. Conceptual Model of Gas Hydrate Growth Conditioned by  
417 Host Sediment Properties, , 104, doi:10.1029/1999JB900175.

418 Cook, A. E., and A. Malinverno (2013), Short migration of methane into a gas hydrate-bearing  
419 sand layer at Walker Ridge, Gulf of Mexico, *Geochemistry, Geophys. Geosystems*, 14(2),  
420 283–291, doi:10.1002/ggge.20040.

421 Cook, A. E., and W. F. Waite (2018), Archie’s Saturation Exponent for Natural Gas Hydrate in  
422 Coarse-Grained Reservoirs, *J. Geophys. Res. Solid Earth*, 123(3),  
423 doi:10.1002/2017JB015138.

424 Cook, A. E., B. I. Anderson, J. Rasmus, K. Sun, Q. Li, T. S. Collett, and D. S. Goldberg (2012),  
425 Electrical anisotropy of gas hydrate-bearing sand reservoirs in the Gulf of Mexico, *Mar.*  
426 *Pet. Geol.*, 34(1), doi:10.1016/j.marpetgeo.2011.09.003.

427 Crutchley, G. J., A. R. Gorman, I. A. Pecher, S. Toulmin, and S. A. Henrys (2011), Geological  
428 controls on focused fluid flow through the gas hydrate stability zone on the southern  
429 Hikurangi Margin of New Zealand, evidenced from multi-channel seismic data, *Mar. Pet.*  
430 *Geol.*, 28(10), 1915–1931, doi:10.1016/j.marpetgeo.2010.12.005.

431 Daigle, H., A. Cook, and A. Malinverno (2015), Permeability and porosity of hydrate-bearing  
432 sediments in the northern Gulf of Mexico, *Mar. Pet. Geol.*, 68, 551–564,  
433 doi:10.1016/j.marpetgeo.2015.10.004.

434 Doser, D. I., and T. H. Webb (2003), Source parameters of large historical (1917-1961)  
435 earthquakes, North Island, New Zealand, *Geophys. J. Int.*, 152(3), 795–832,  
436 doi:10.1046/j.1365-246X.2003.01895.x.

437 Fagereng, Å., H. M. Savage, J. K. Morgan, M. Wang, F. Meneghini, P. M. Barnes, R. Bell, H.  
438 Kitajima, D. D. McNamara, and D. M. Saffer (2019), Mixed deformation styles observed on  
439 a shallow subduction thrust, Hikurangi margin, New Zealand, *Geology*, 47(9), 1–5,  
440 doi:10.1130/G46367.1/4797825/g46367.pdf.

441 Geersen, J., F. Scholz, P. Linke, M. Schmidt, D. Lange, J. Behrmann, D. Volker, and C. Hensen  
442 (2016), Fault zone controlled seafloor methane seepage in the rupture area of the 2010  
443 Maule earthquake, Central Chile, *Geochemistry, Geophys. Geosystems*, 17, 4802–4813,  
444 doi:10.1002/2015GC006171.Received.

445 Goldberg, D. S., R. L. Kleinberg, J. L. Weinberger, A. Malinverno, P. J. McLellan, and T. S.  
446 Collett (2010), 16. Evaluation of Natural Gas-Hydrate Systems Using Borehole Logs,  
447 *Geophys. Charact. Gas Hydrates*, 239–261, doi:10.1190/1.9781560802197.ch16.

448 Gray, M., R. E. Bell, J. V. Morgan, S. Henrys, and D. H. N. Barker (2019), Imaging the Shallow  
449 Subsurface Structure of the North Hikurangi Subduction Zone, New Zealand, Using 2-D  
450 Full-Waveform Inversion, *J. Geophys. Res. Solid Earth*, 124(8), 9049–9074,  
451 doi:10.1029/2019JB017793.

452 Hyndman, R. D., M. Yamano, and D. A. Oleskevich (1997), The seismogenic zone of  
453 subduction thrust faults, *Isl. Arc*, 6(3), 244–260, doi:10.1111/j.1440-1738.1997.tb00175.x.

454 Ide, S., A. Baltay, and G. C. Beroza (2011), Shallow Dynamic Overshoot and Energetic Deep  
455 Rupture in the 2011, *Science (80-. )*, 332, 1426–1430, doi:10.1126/science.1207020.

456 Kastner, M., K. A. Kvenvolden, and T. D. Lorenson (1998), Chemistry, isotopic composition,  
457 and origin of a methane-hydrogen sulfide hydrate at the Cascadia subduction zone, *Earth*  
458 *Planet. Sci. Lett.*, 156(3–4), 173–183, doi:10.1016/S0012-821X(98)00013-2.

459 Kastner, M., E. A. Solomon, R. N. Harris, and M. E. Torres (2014), Fluid Origins, Thermal  
460 Regimes, and Fluid and Solute Fluxes in the Forearc of Subduction Zones, in *Developments*  
461 *in Marine Geology, Volume 7*, pp. 671–733.

462 Kim, G. Y., B. Narantsetseg, B. J. Ryu, D. G. Yoo, J. Y. Lee, H. S. Kim, and M. Riedel (2013),  
463 Fracture orientation and induced anisotropy of gas hydrate-bearing sediments in seismic  
464 chimney-like-structures of the Ulleung Basin, East Sea, *Mar. Pet. Geol.*, 47, 182–194,  
465 doi:10.1016/j.marpetgeo.2013.06.001.

466 Kinoshita, C. et al. (2018), Changes in Physical Properties of the Nankai Trough Megasplay  
467 Fault Induced by Earthquakes, Detected by Continuous Pressure Monitoring, *J. Geophys.*  
468 *Res. Solid Earth*, 123(2), 1072–1088, doi:10.1002/2017JB014924.

469 Kroeger, K. F., A. Plaza-Faverola, P. M. Barnes, and I. A. Pecher (2015), Thermal evolution of  
470 the New Zealand Hikurangi subduction margin: IMPACT on natural gas generation and  
471 methane hydrate formation - A model study, *Mar. Pet. Geol.*, 63, 97–114,  
472 doi:10.1016/j.marpetgeo.2015.01.020.

473 Luthi, S. (2001), *Geological Well Logs: Their Use in Reservoir Modeling*, Springer-Verlag  
474 Berlin Heidelberg.

475 Malinverno, A. (2010), Marine gas hydrates in thin sand layers that soak up microbial methane,  
476 *Earth Planet. Sci. Lett.*, 292(3–4), 399–408, doi:10.1016/j.epsl.2010.02.008.

477 Malinverno, A., and D. S. Goldberg (2015), Testing short-range migration of microbial methane  
478 as a hydrate formation mechanism: Results from Andaman Sea and Kumano Basin drill  
479 sites and global implications, *Earth Planet. Sci. Lett.*, 422, 105–114,  
480 doi:10.1016/j.epsl.2015.04.019.

481 Moore, J. C., and P. Vrolijk (1992), Fluids in accretionary prisms, *Rev. Geophys.*, 30(2), 113–  
482 135, doi:https://doi.org/10.1029/92RG00201.

483 Moore, J. C., G. F. Moore, G. R. Cochrane, and H. J. Tobin (1995), Negative-polarity seismic  
484 reflections along faults of the Oregon accretionary prism: indicators of overpressuring, *J.*  
485 *Geophys. Res.*, 100(B7), doi:10.1029/94jb02049.

486 Nimblett, J., and C. Ruppel (2003), Permeability evolution during the formation of gas hydrates  
487 in marine sediments, *J. Geophys. Res. Solid Earth*, 108(B9), 1–17,  
488 doi:10.1029/2001jb001650.

489 Nole, M., H. Daigle, A. E. Cook, J. I. T. Hillman, and A. Malinverno (2017), Linking basin-scale  
490 and pore-scale gas hydrate distribution patterns in diffusion-dominated marine hydrate  
491 systems, *Geochemistry, Geophys. Geosystems*, 18, 653–675, doi:10.1002/2016GC006662.

492 Pearson, C. F., P. M. Halleck, P. L. McGuire, R. Hermes, and M. Mathews (1983), Natural gas  
493 hydrate deposits: a review of in situ properties, *J. Phys. Chem.*, 87(21), 4180–4185,  
494 doi:10.1021/j100244a041.

495 Pecher, I. A. et al. (2010), Focussed fluid flow on the Hikurangi Margin, New Zealand -  
496 Evidence from possible local upwarping of the base of gas hydrate stability, *Mar. Geol.*,  
497 272(1–4), 99–113, doi:10.1016/j.margeo.2009.10.006.

498 Plaza-Faverola, A., D. Klaeschen, P. Barnes, I. Pecher, S. Henrys, and J. Mountjoy (2012),  
499 Evolution of fluid expulsion and concentrated hydrate zones across the southern Hikurangi  
500 subduction margin, New Zealand: An analysis from depth migrated seismic data,  
501 *Geochemistry, Geophys. Geosystems*, 13(8), doi:10.1029/2012GC004228.

502 Priegnitz, M., J. Thaler, E. Spangenberg, J. M. Schicks, J. Schrötter, and S. Abendroth (2015),  
503 Characterizing electrical properties and permeability changes of hydrate bearing sediments  
504 using ERT data, *Geophys. J. Int.*, 202(3), 1599–1612, doi:10.1093/gji/ggv245.

505 Rempel, A. W. (2011), A model for the diffusive growth of hydrate saturation anomalies in  
506 layered sediments, *J. Geophys. Res. Solid Earth*, 116(10), 1–15,  
507 doi:10.1029/2011JB008484.

508 Riedel, M., T. S. Collett, P. Kumar, A. V. Sathe, and A. Cook (2010), Seismic imaging of a  
509 fractured gas hydrate system in the Krishna-Godavari Basin offshore India, *Mar. Pet. Geol.*,  
510 27(7), doi:10.1016/j.marpetgeo.2010.06.002.

511 Rogers, G., and H. Dragert (2003), Episodic Tremor and Slip on the Cascadia Subduction Zone,  
512 *Science* (80-. ), 300, 1942–1944, doi:10.1126/science.1084783.

513 Saffer, D. M., and H. J. Tobin (2011), Hydrogeology and Mechanics of Subduction Zone  
514 Forearcs: Fluid Flow and Pore Pressure, *Annu. Rev. Earth Planet. Sci.*, 39(1), 157–186,  
515 doi:10.1146/annurev-earth-040610-133408.

516 Saffer, D. M., and L. M. Wallace (2015), The frictional, hydrologic, metamorphic and thermal  
517 habitat of shallow slow earthquakes, *Nat. Geosci.*, 8(8), 594–600, doi:10.1038/ngeo2490.

518 Saffer, D. M., L. M. Wallace, P. M. Barnes, I. A. Pecher, K. E. Petronotis, L. J. LeVay, and  
519 the E. 372/375 Scientists (2019a), Expedition 372B / 375 summary, *Proc. Int. Ocean  
520 Discov. Progr. Vol. 372B/375, 372B/375*,  
521 doi:https://doi.org/10.14379/iodp.proc.372B375.101.2019.

522 Saffer, D. M. et al. (2019b), Site U1518, *Proc. Int. Ocean Discov. Progr. Vol. 372B/375,*  
523 *372B/375*.

524 Sawyer, A. H., P. Flemings, D. Elsworth, and M. Kinoshita (2008), Response of submarine  
525 hydrologic monitoring instruments to formation pressure changes: Theory and application  
526 to Nankai advanced CORKs, *J. Geophys. Res. Solid Earth*, 113(1), 1–16,  
527 doi:10.1029/2007JB005132.

528 Schlumberger (2007), *geoVISION: Resistivity imaging for productive drilling*.

529 Screaton, E. et al. (2009), Interactions between deformation and fluids in the frontal thrust region  
530 of the NanTroSEIZE transect offshore the Kii Peninsula, Japan: Results from IODP  
531 Expedition 316 Sites C0006 and C0007, *Geochemistry, Geophys. Geosystems*, 10(12),  
532 doi:10.1029/2009GC002713.

533 Sloan, E. D., and C. Koh (2007), *Clathrate Hydrates of Natural Gases, Third Edition*, Chemical  
534 Industries, CRC Press.

535 Spangenberg, E. (2001), Modeling of the influence of gas hydrate content on the electrical  
536 properties of porous sediments, *J. Geophys. Res. Solid Earth*, 106, 6535–6548.

537 Sultan, N. (2007), Comment on “Excess pore pressure resulting from methane hydrate  
538 dissociation in marine sediments: A theoretical approach” by Wenye Xu and Leonid N.  
539 Germanovich, *J. Geophys. Res. Solid Earth*, 112(2), 1–7, doi:10.1029/2006JB004527.

540 Vanderbeek, B. P., and A. W. Rempel (2018), On the Importance of Advective Versus Diffusive  
541 Transport in Controlling the Distribution of Methane Hydrate in Heterogeneous Marine  
542 Sediments, , 1, doi:10.1029/2017JB015298.

543 Waite, W. F. et al. (2009), Physical properties of hydrate-bearing sediments, *Rev. Geophys.*,  
544 47(4), 1–38, doi:10.1029/2008RG000279.

545 Wallace, L. M. et al. (2009), Characterizing the seismogenic zone of a major plate boundary  
546 subduction thrust: Hikurangi Margin, New Zealand, *Geochemistry, Geophys. Geosystems*,  
547 doi:10.1029/2009GC002610.

548 Wallace, L. M., J. Beavan, S. Bannister, and C. Williams (2012), Simultaneous long-term and  
549 short-term slow slip events at the Hikurangi subduction margin , New Zealand :  
550 Implications for processes that control slow slip event occurrence , duration , and migration,  
551 *J. Geophys. Res. Solid Earth*, *117*, 1–18, doi:10.1029/2012JB009489.

552 Wallace, L. M., S. C. Webb, Y. Ito, K. Mochizuki, R. Hino, S. Henrys, S. Y. Schwartz, and A. F.  
553 Sheehan (2016), Slow slip near the trench at the Hikurangi subduction zone, New Zealand,  
554 *Science* (80-. ), *352*(6286), 1–5.

555 Wallace, L. M., D. M. Saffer, P. M. Barnes, I. A. Pecher, K. E. Petronotis, A. LeVay, L.J., and  
556 and the E. 372/375 S. Proceedings (2019), Expedition 372B/375 methods, , *372B/375*.

557 Watson, S. J. et al. (2019), Focused fluid seepage related to variations in accretionary wedge  
558 structure, Hikurangi margin, New Zealand, *Geology*, *48*(1), 56–61, doi:10.1130/G46666.1.

559 Weinberger, J. L., and K. M. Brown (2006), Fracture networks and hydrate distribution at  
560 Hydrate Ridge, Oregon, *Earth Planet. Sci. Lett.*, *245*(1–2), 123–136,  
561 doi:10.1016/j.epsl.2006.03.012.

562 Xu, W., and L. N. Germanovich (2006), Excess pore pressure resulting from methane hydrate  
563 dissociation in marine sediments: A theoretical approach, *J. Geophys. Res. Solid Earth*,  
564 *111*(1), 1–12, doi:10.1029/2004JB003600.

565 Yun, T. S., F. M. Francisca, J. C. Santamarina, and C. Ruppel (2005), Compressional and shear  
566 wave velocities in uncemented sediment containing gas hydrate, *Geophys. Res. Lett.*,  
567 *32*(10), 1–5, doi:10.1029/2005GL022607.

568

569